


Large-scale volumetric pressure from tomographic PTV with HFSB tracers

Jan F. G. Schneiders¹  · Giuseppe C. A. Caridi¹ · Andrea Sciacchitano¹ · Fulvio Scarano¹

Received: 17 June 2016 / Revised: 29 July 2016 / Accepted: 13 September 2016 / Published online: 13 October 2016
© The Author(s) 2016. This article is published with open access at Springerlink.com

Abstract The instantaneous volumetric pressure in the near-wake of a truncated cylinder is measured by use of tomographic particle tracking velocimetry (PTV) using helium-filled soap bubbles (HFSB) as tracers. The measurement volume is several orders of magnitude larger than that reported in tomographic experiments dealing with pressure from particle image velocimetry (PIV). The near-wake of a truncated cylinder installed on a flat plate ($Re_D = 3.5 \times 10^4$) features both wall-bounded turbulence and large-scale unsteady flow separation. The instantaneous pressure is calculated from the time-resolved 3D velocity distribution by invoking the momentum equation. The experiments are conducted simultaneously with surface pressure measurements intended for validation of the technique. The study shows that time-averaged pressure and root-mean-squared pressure fluctuations can be accurately measured both in the fluid domain and at the solid surface by large-scale tomographic PTV with HFSB as tracers, with significant reduction in manufacturing complexity for the wind-tunnel model and circumventing the need to install pressure taps or transducers. The measurement over a large volume eases the extension toward the free-stream regime, providing a reliable boundary condition for the solution of the Poisson equation for pressure. The work demonstrates, in the case of the flow past a truncated cylinder, the use of HFSB tracer particles for pressure

measurement in air flows in a measurement volume that is two orders of magnitude larger than that of conventional tomographic PIV.

Volumetric and surface pressure measurements have become possible from tomographic particle image velocimetry (PIV) measurements as reviewed in van Oudheusden (2013). The appealing aspect of the approach is that it avoids the requirement of instrumentation of wind-tunnel models using pressure transducers. Pressure-sensitive paint (PSP; Bitter et al. 2012) offers similar advantages being less intrusive; however, its use in the low-speed regime is hampered by the low sensitivity of PSP. A recent study, based on a numerically simulated experiment, has compared several existing methods that obtain pressure-from-PIV data (Blinde et al. 2016). Results were fairly equivalent, which indicates the maturity of pressure-from-PIV techniques. On the other hand, all studies involving pressure-from-PIV in air have dealt with a fairly limited size of the measurement volume of a few cubic centimeters, mostly due to the low intensity of the light scattered by micron-size tracers for tomographic PIV, even when a multi-pass light amplification system is employed (Ghaemi and Scarano 2010). For example, despite the use of this system by Ghaemi and Scarano (2013) for pressure extraction from time-resolved tomographic PIV, only a $1.6 \times 0.6 \times 2.4 \text{ cm}^3$ measurement volume was achieved in a turbulent boundary layer at 10 m/s. The advantage of tomographic PIV with such small measurement volumes is the relatively good spatial resolution that it offers. However, very few time-resolved tomographic PIV experiments, mainly in water, are reported in the literature where both the region of interest (typically rotational) and an irrotational region are included in the measurement volume (e.g. Jeon et al. 2016). Due to the

Electronic supplementary material The online version of this article (doi:10.1007/s00348-016-2258-x) contains supplementary material, which is available to authorized users.

✉ Jan F. G. Schneiders
J.F.G.Schneiders@tudelft.nl

¹ Department of Aerospace Engineering, TU Delft, Delft, The Netherlands

limited measurement volume size especially for measurements in air flows, it is typically not possible to include an irrotational region in the measurement domain. As a result, boundary conditions for the pressure Poisson equation may need to be imposed in rotational or turbulent regions (e.g. Pröbsting et al. 2013). Applying reliable boundary conditions is of importance for the accuracy of the solution (van Oudheusden 2013), which limits the applicability of today's pressure-from-PIV techniques to large-scale and industry-relevant wind-tunnel experiments.

Recent advances of tomographic PIV using helium-filled soap bubbles (HFSB) as tracers have shown that the measurement volume can be significantly increased for velocity measurements in air (Kühn et al. 2011). The application in wind tunnels is possible (Scarano et al. 2015), but remains hampered by the limited seeding concentration due to limitations on tracer particle generation (Caridi et al. 2015). The limited tracer particle seeding concentration motivates the use of particle tracking techniques for processing of the time-resolved and volumetric data, as recent studies (e.g. Schanz et al. 2016; Schneiders and Scarano 2016) have showed increased spatial resolution in such cases. The spatial resolution of the instantaneous velocity fields becomes on the order of the inter-particle distance. Furthermore, statistics of the flow field are obtained by ensemble averaging the PTV results, and hence, spatial resolution of the statistics can be increased by increasing the observation time at constant seeding concentration (Kähler et al. 2012).

In the present study, an experiment is realized where the time-averaged pressure and root-mean-squared (rms) pressure fluctuations are characterized. The instantaneous pressure distribution as well as its frequency spectra is extracted and compared with reference measurements obtained with surface pressure transducers. The flow past a truncated cylinder installed on a flat plate is considered, which exhibits pressure fluctuations due to both wall-bounded turbulence and large-scale unsteady separation. This configuration was considered in a variety of studies, reviewed in Sumner (2013), and is relevant for applications within the field of aerodynamics (e.g. car side mirror or aircraft landing gear), which involve issues related to flow-induced vibration and aero-acoustics noise. The measurement of the instantaneous surface pressure in this flow case was proven to be a challenge, with recent studies employing wind-tunnel models equipped with up to 179 simultaneously operated pressure taps (Dobriloff and Nitsche 2009).

The experiment is conducted in a low-speed wind tunnel with $40 \times 40\text{-cm}^2$ cross section. A cylinder of 10-cm diameter, D , and equal height, h , is installed on a flat plate. Measurements are conducted at a Reynolds number based on the cylinder diameter of $Re_D = 3.5 \times 10^4$ (free-stream velocity of 5 m/s). A tripping device past the leading edge of the ground plate forces laminar to turbulent transition. A

tripping element was placed 10 cm downstream of the leading edge and 50 cm upstream of the cylinder. The boundary layer thickness, δ_{99} , at the cylinder mounting location (with the cylinder removed) is 1.5 cm. The literature shows that the local relative boundary thickness to the cylinder height ($\delta_{99}/h = 0.15$) and the aspect ratio of the cylinder ($h/D = 1$) play an important role in the wake development. The boundary layer in the current experiment is classified as a thin boundary layer (Bourgeois et al. 2011; Sumner 2013, and references therein). For details regarding the wake development, the reader is referred to the aforementioned literature. The near-wake of the cylinder is captured within a measurement volume of $20 \times 17 \times 18\text{ cm}^3$ (6 L). In comparison, for measurements over a truncated cylinder with a diameter of 6 cm and a height of 13 cm, Hain et al. (2008) focused on the flow region on the top of the cylinder with a volume of $8 \times 8 \times 1\text{ cm}^3$ (0.06 L) in a water tunnel with a low-repetition rate tomographic PIV system. Figure 1 left illustrates the measurement volume (shaded green) in the test section. The test section channel is cut-out in the figure to illustrate the cylinder and the measurement volume. Achieving this measurement domain was only possible using HFSB as tracers, with a diameter of approximately $300\text{ }\mu\text{m}$ and in the neutrally buoyant regime. Scarano et al. (2015) report a relaxation time τ_{HFSB} for the HFSB tracer particles of below $50\text{ }\mu\text{s}$. With a typical vorticity magnitude peak value of $\omega_p = 1000\text{ Hz}$ measured in the present experiment, the turnover time of the vortices is approximated at $1/\omega_p = 1\text{ ms}$. Using this time scale, the Stokes number of the tracers is $\text{Stk} = \tau_{\text{HFSB}}/\tau_{\text{flow}} \leq 0.05$, which is below the threshold of 0.1 reported by Tropea et al. (2007) for accurate tracking fidelity. In addition, with a typical Lagrangian acceleration, a , of 300 m/s^2 in the present flow (evaluated from the particle tracking results), the slip velocity is on the order of $u_{\text{slip}} \approx \tau \times a = 15\text{ mm/s}$, which is 0.3 % of the free-stream velocity.

Three sequences of 2000 single-frame images are acquired at 2 kHz to obtain a time-resolved measurement. An example of a recorded particle image by one of the cameras is given in Fig. 1, right. Gaussian smoothing with a 3×3 pixel kernel was applied to the image for clarity of the visualization. In the supplementary material attached to this paper, a movie of a sequence of particle images is given. The particle density was approximately 0.7 bubbles per cm^3 , and the resulting particle image source density equals 0.008 particles per pixel (ppp). The recorded images were preprocessed using a time-minimum subtraction filter and subsequently Gaussian smoothing with a 3×3 pixel kernel. The particle images are reconstructed using 6 iterations of the FastMART algorithm in the LaVision Davis 8.2 software package. The SNR of the reconstruction, calculated from the averaged z -intensity, profile is in the order of 100, significantly larger than values for tomographic PIV

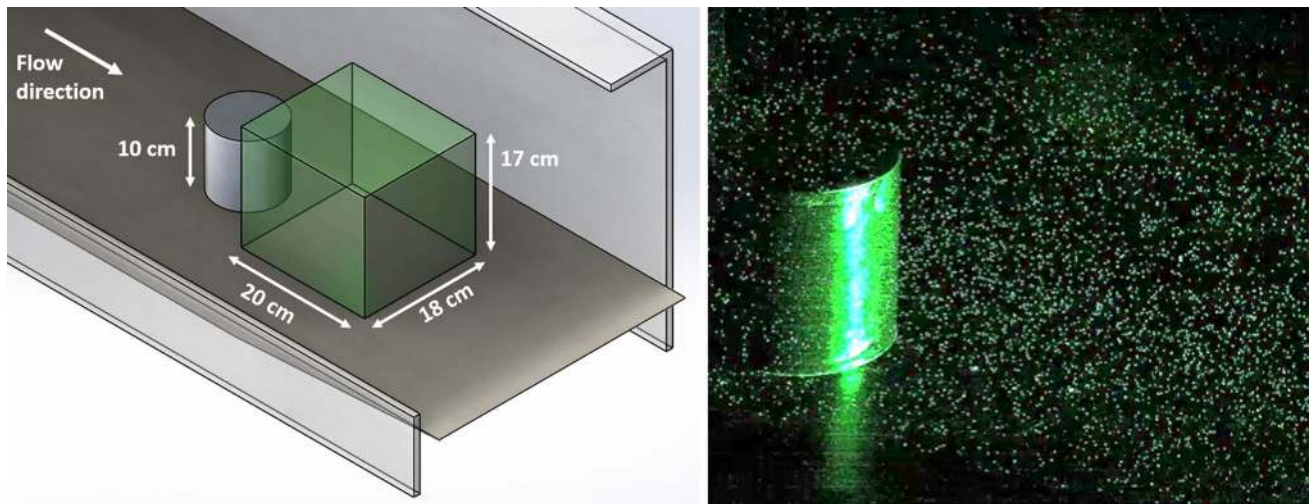


Fig. 1 Schematic of the setup in the test section, with measurement volume shaded in *green* and channel cut-out for clarity (*left*) and an example of one of the instantaneous images captured (*right*)

Table 1 Tomographic measurement setup

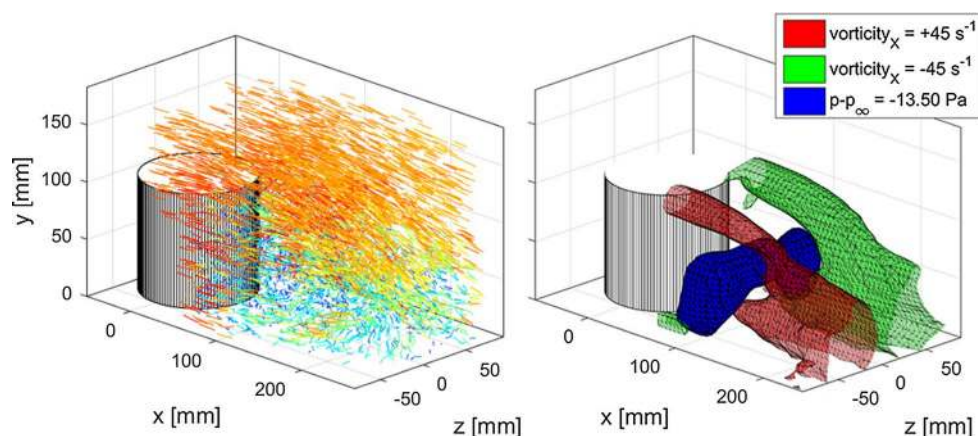
Measurement volume	$20 \times 17 \times 18 \text{ cm}^3$ (6 L)
Seeding	Helium-filled soap bubbles (HFSB) 300- μm diameter
Illumination	Quantronix Darwin-Duo Nd:YLF laser Pulse energy $2 \times 25 \text{ mJ}$ at 1 kHz
Recording devices	4 \times Photron FastCAM SA1 CMOS, 1024×1024 pixels, 12-bit, 20- μm pixel size
Imaging	$f = 105\text{-mm}$ Nikon objectives (aperture $f/16$)
Acquisition frequency	2000 Hz (single-frame mode)
Number of frames recorded	3 \times 2000

experiments (2–5) due to the low seeding concentration and large amount of light scattered by the HFSB. Further details of the measurement setup are given in Table 1.

Particles are identified in the reconstructed objects by peak finding of peak intensity values in a $5 \times 5 \times 5$ vox ($1.3 \times 1.3 \times 1.3 \text{ mm}^3$) neighborhood. Approximately 10^{-5} particles per voxel (ppv) are present. Sub-voxel accuracy of particle location is obtained by fitting of a 3D Gaussian through the peak intensity distribution. The identified particles have a typical radius (standard deviation of the Gaussian peak fit) of $\sigma_x = \sigma_y = 0.4$ and $\sigma_z = 0.6$ vox. The elongation of the particles in depth direction is expected for tomographic reconstructions (Elsinga et al. 2006), and positional error on the particle position can potentially be reduced using novel reconstruction techniques (e.g. iterative particle reconstruction, IPR; Wieneke 2013) and particle tracking algorithms (e.g. ‘Shake-the-Box’; Schanz et al. 2016). A particle tracking algorithm based on Malik et al. (1993) is used to build the trajectory of individual particles. A five-snapshot track length is employed, through which

a third order polynomial is fitted. The time derivative of each polynomial yields velocity at the particle locations. A visualization of the instantaneous particle trajectories is given in Fig. 2, left, where the tracks are colored by velocity magnitude. Low-speed particles (blue) are visible in the wake region and high-speed particles (red) in the outer flow. Velocity is subsequently calculated on a computational grid ($200 \times 170 \times 180 \text{ mm}^3$) by the adaptive Gaussian windowing (AGW; Agüí and Jiménez 1987) technique. The standard deviation of the Gaussians was set to the average inter-particle distance of 6 mm, and 75 % overlap was used. The AGW interpolator acts as a Gaussian weighted sliding average filter. The recent study by Schneiders and Scarano (2016) shows that a better recovery of the magnitude of the turbulent velocity fluctuations can be obtained using more advanced and computationally expensive interpolators that incorporate constraints from flow physics (e.g. ‘VIC+’: Schneiders and Scarano 2016; ‘FlowFit’: Gesemann et al. 2016). However, the AGW technique was chosen in the present study for its computational efficiency

Fig. 2 Visualization of particle tracks (color coded by velocity magnitude, left). Isosurfaces of time-averaged streamwise vorticity and pressure in the separated region (right)



and established position in the community. It should be remarked that with more advanced techniques potentially lower modulation of the velocity fields and pressure gradient fields could be obtained, thus enhancing the spatial resolution of the instantaneous pressure fields shown later in this manuscript.

Instantaneous pressure, p , is calculated by solving the Poisson equation for pressure (see e.g. van Oudheusden 2013),

$$\nabla^2 p = \nabla \cdot \left(-\rho \frac{D\mathbf{u}}{Dt} + \mu \nabla^2 \mathbf{u} \right), \quad (1)$$

with von Neumann (pressure gradient) boundary conditions from the momentum equation on all volume boundaries except the top side, where a Dirichlet boundary condition calculated from the Bernoulli equation is specified. It is verified that the flow at the upper boundary of the measurement is irrotational by visualizing the vorticity distribution. The velocity material derivative is evaluated using the Lagrangian technique by Pröbsting et al. (2013).

Time-averaged pressure, \bar{p} , is evaluated using the Reynolds-averaged approach outlined in van Oudheusden (2013),

$$\nabla^2 \bar{p} = -\rho \nabla \cdot (\bar{\mathbf{u}} \cdot \nabla) \bar{\mathbf{u}} - \rho \nabla \cdot \nabla \cdot (\overline{\mathbf{u}'\mathbf{u}'}). \quad (2)$$

The instantaneous velocity fields are limited in spatial resolution by the tracer particle concentration. To obtain the time-averaged velocity field and the turbulence statistics at a higher spatial resolution, all instantaneous and scattered velocity vectors found from the PTV procedure are ensemble averaged in Gaussian interrogation windows with standard deviation $\sigma = 5$ mm. An overlap of the Gaussian windows of 75 % overlap is used. The resulting time-averaged flow field shows two counter-rotating tip vortices emerging from the truncated cylinder (Fig. 2, right). This vortex pair is expected in the time-averaged field (Sumner 2013), but it should be remarked that the

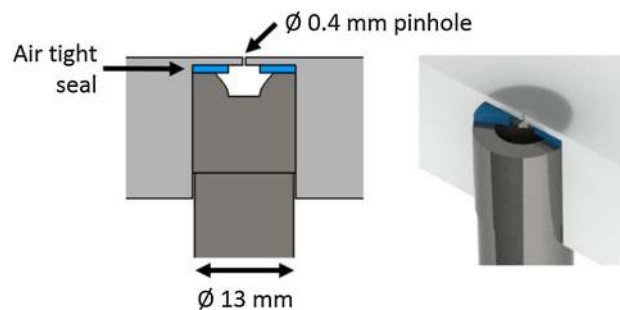


Fig. 3 Schematic of the microphone installation for reference measurements of instantaneous pressure. The isometric view (right) is cut-out in the figure

literature (Hain et al. 2008; Bourgeois et al. 2011; among others) shows that the instantaneous velocity fields do not show one single vortex pair but a more complex flow field.

The simultaneous measurement of the surface pressure fluctuations with surface pressure transducers provides a ground truth to estimate the accuracy of the proposed measurements. The instantaneous and time-averaged measurements are taken using, respectively, a LinearX M51 microphone and a Mensor (type 2101). The installation of the microphones is sketched in Fig. 3. Both transducers are mounted under a 0.4-mm-diameter pinhole. The acquisition frequency of the microphones is set to 10 kHz, and the calibration-corrected frequency response is ± 1 dB in the range 10 Hz–40 kHz. The length of the microphones (10.8 cm) indicates potential difficulty when instrumenting wind-tunnel models, which shows again the relevance of pressure-from-PIV approaches. The synchronization between microphone and tomographic PIV measurements is obtained recording the laser trigger signal on an additional channel of the data acquisition system. For the time-averaged pressure measurements, the Mensor signal is recorded at 10 Hz for a duration of 2 min.

Fig. 4 Time-averaged surface pressure; surface pressure transducer measurements (*left*) and tomographic PTV with HFSB tracers (*right*). The *dashed red lines* correspond to the profiles plotted in Fig. 5. *Colorbar* values above $p - p_\infty = 5$ Pa are saturated and shown in *dark red* for clarity

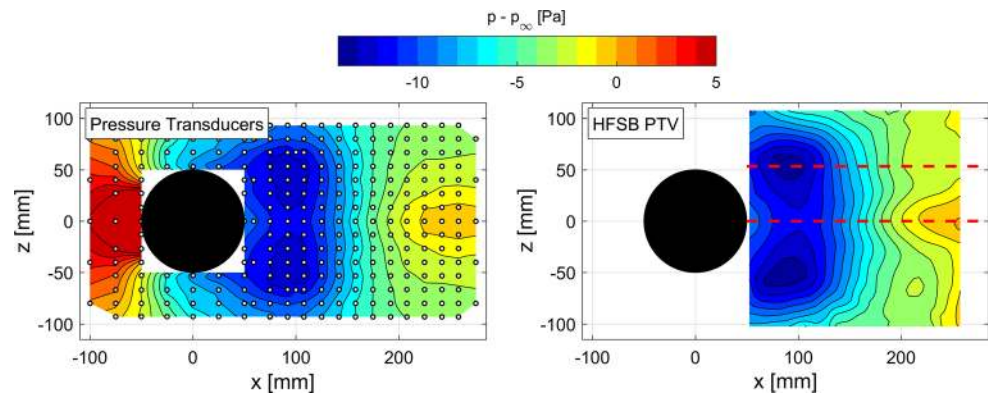
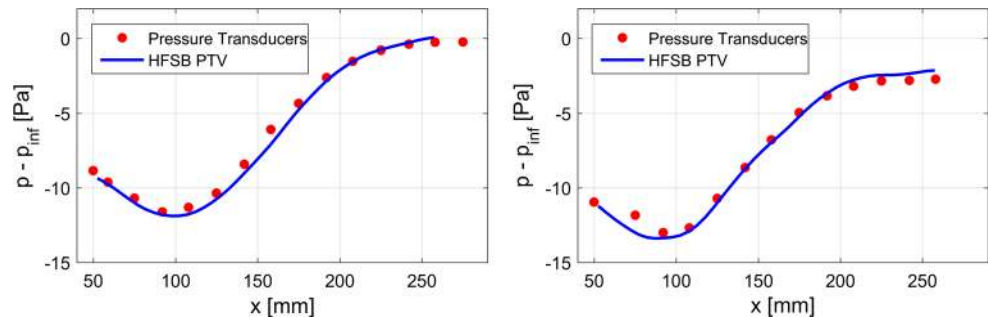


Fig. 5 Time-averaged surface pressure along $z = 0$ mm (*left*) and $z = 53.3$ mm (*right*). The cylinder is centered at $x = 0$ mm as shown in Fig. 4



The surface pressure is mapped on an array of 263 measurement positions obtained with pressure transducers. These measurements are obtained by moving the cylinder relative to 20 sensors arranged on a grid with steps of 17 mm and 13.5 mm in streamwise and spanwise directions, respectively. The measurement encompasses the stagnation region ahead of the cylinder area and the wake (Fig. 4, left). The results illustrate the expected pressure increase near the stagnation point and a lower pressure region in the cylinder wake. Two pressure minima are found in the wake of the cylinder, which are attributed to the presence of an arch-vortex in the time-averaged flow field (Pattenden et al. 2005). The results obtained from the tomographic experiment are shown in Fig. 4, right. The measurements cover the wake region, and the spatial distribution of pressure follows closely the distribution obtained with the surface pressure transducers and reproduces both the two pressure minima and the maximum after reattachment. The pressure reconstruction by large-scale tomographic PTV in addition provides pressure in the full measurement volume. Figure 2, right shows an arch-shaped low-pressure region (blue isosurface) in the near-wake, which is consistent with the two minima in the surface pressure observed above.

A quantitative comparison is made extracting two streamwise profiles. Figure 5 shows the mean surface pressure along the centerline $z = 0$ mm (left) and along the line at $z = 53.3$ mm (right). The position of these lines is indicated in Fig. 3, right (dashed red lines). The minimum

pressure ($p - p_\infty = -12$ Pa) is reached at approximately $x = 100$ mm. On both profiles, a good agreement is found between the two measurements, with a discrepancy in the order of 0.5 Pa.

The measurement and assessment of instantaneous pressure fluctuations by tomographic PIV have shown to pose a formidable challenge within a number of experiments (de Kat and van Oudheusden 2012; Ghaemi and Scarano 2013; Pröbsting et al. 2013). The rms fluctuations of the surface pressure estimated with tomographic PTV are compared here to the results obtained with the surface-mounted microphone. Two profiles along z are illustrated in Fig. 6. Two peaks of pressure fluctuations correspond to the shear layer locations. Comparing the profiles at $x = 100$ and 150 mm, the amplitude of the rms fluctuations decreases and the distribution becomes flatter moving downstream. The comparison of tomographic PTV results and that obtained with the microphone show that the former slightly overestimates by about 0.5 Pa the rms fluctuations in minimum region at the symmetry plane. Some discrepancy is also observed at the edge of the domain (marked by the dashed black line).

A relevant aspect of unsteady pressure measurements relates to the frequency content of the fluctuations. In this respect, tomographic PTV offers the potential of a field measurement that can be further analyzed in modes using proper orthogonal decomposition (POD) or dynamic mode decomposition (DMD). The time-resolved measurement of

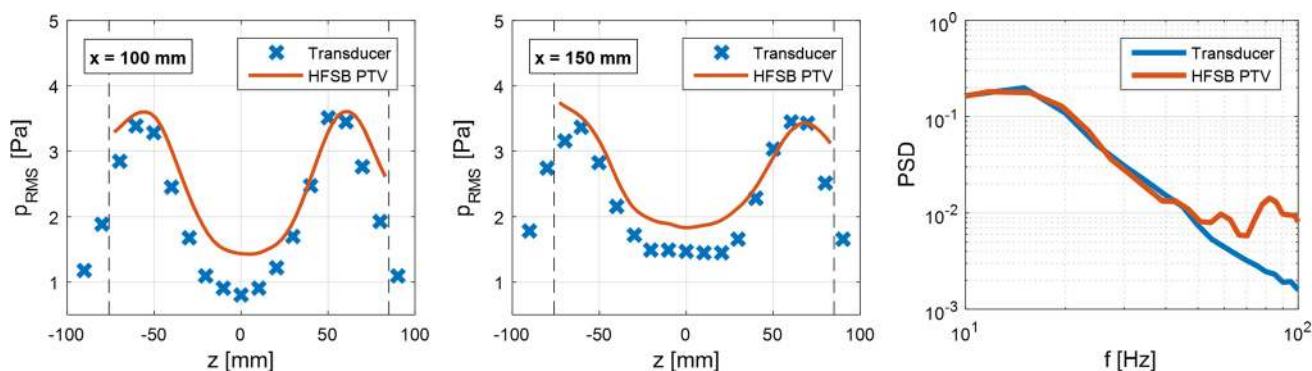


Fig. 6 Surface RMS pressure fluctuations at $x = 100$ mm (left) and $x = 150$ mm (middle) and power spectral density of surface pressure fluctuations at $x = 100$ mm and $z = 30$ mm (right)

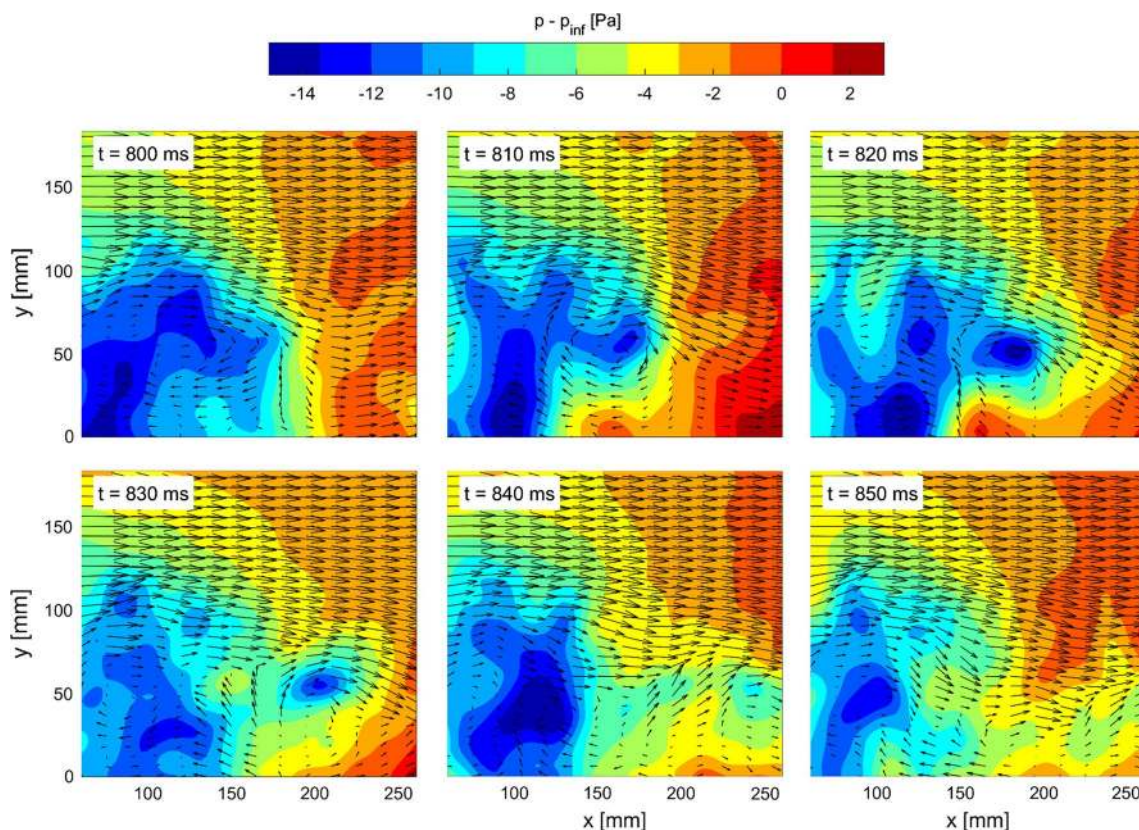


Fig. 7 Time series of instantaneous pressure in the plane $z = 50$ mm. The in-plane velocity vectors are subsampled for clarity

the surface pressure at a point is used to evaluate its power spectral density (Fig. 6, right). The spectrum is calculated using Welch’s method using 0.25 s Hamming windows. No signal processing has been applied to the signals, other than the anti-alias filter within the pressure transducer acquisition system which has negligible effects because of the relatively high acquisition frequency. A broad peak is seen around 15 Hz, and the spectrum obtained with tomographic PTV follows that measured by the microphone with good agreement up to 50 Hz. For higher frequencies,

the measurement error seems to dominate the PTV result, which “peels off” the reference data and remains approximately constant. The errors in the present measurement are considered to be dominated by the low seeding concentration and consequently too limited spatial resolution to resolve small-scale structures and fluctuations. When the signals are band-pass filtered between 10 and 100 Hz, the cross-correlation peak between the microphone and tomographic PTV results is approximately 0.6. This value corresponds to that reported in other studies that evaluate

pressure-from-PIV (de Kat and van Oudheusden 2012; Ghaemi and Scarano 2013; Pröbsting et al. 2013).

Finally, the instantaneous pressure visualization in the flow field and at the solid surface offers the opportunity to correlate the pressure fluctuations to the activity of large-scale coherent structures in the flow. Figure 7 shows a short sample of a sequence, where the pressure spatiotemporal evolution in a plane ($z = 50$ mm) is displayed along with the velocity field that visualizes vortex shedding. The supplementary material added to the manuscript shows a video animation of the pressure spatiotemporal evolution. As mentioned above, the time-resolved flow field does not simplify to two counter-rotating tip vortices shown in the time-averaged flow field. For detailed understanding of the flow field in the near-wake, the reader is referred to Bourgeois et al. (2011) and the references within the review paper by Sumner (2013).

In conclusion, the present study shows the use of large-scale tomographic PTV with HFSB tracers for the evaluation of the time-averaged and instantaneous volumetric pressure distribution. The measurement domain is more than two orders of magnitude larger than that obtained with tomographic PIV using conventional tracers. Despite the relatively low concentration of the tracers, the tomographic PTV approach reconstructs the velocity and pressure fields, yielding a highly accurate mean pressure distribution and rms fluctuations with reasonable accuracy. The HFSB tracer particles have demonstrated their use for measurement of pressure in a large measurement volume of 6 L, in the case of the flow past a surface-mounted truncated cylinder at $Re_D = 3.5 \times 10^4$.

Acknowledgments This research is partly funded by LaVision GmbH.

Open Access This article is distributed under the terms of the Creative Commons Attribution 4.0 International License (<http://creativecommons.org/licenses/by/4.0/>), which permits unrestricted use, distribution, and reproduction in any medium, provided you give appropriate credit to the original author(s) and the source, provide a link to the Creative Commons license, and indicate if changes were made.

References

- Agüí JC, Jiménez J (1987) On the performance of particle tracking. *J Fluid Mech* 185:447–468. doi:10.1017/S0022112087003252
- Bitter M, Hara T, Hain R, Yorita D, Asai K, Kähler CJ (2012) Characterization of pressure dynamics in an axisymmetric separating/reattaching flow using fast-responding pressure-sensitive paint. *Exp Fluids* 53:1737–1749. doi:10.1007/s00348-012-1380-7
- Blinde P, Michaelis D, van Oudheusden BW, Weiss P-E, de Kat R, Laskari A, Jeon YJ, David L, Schanz D, Huhn F, Gesemann S, Novara M, McPhaden C, Neeteson N, Rival D, Schneiders JFG, Schrijer F (2016) Comparative assessment of PIV-based pressure evaluation techniques applied to a transonic base flow. In: 18th international symposium on the application of laser techniques to fluid mechanics. Lisbon, Portugal, 4–7 July
- Bourgeois JA, Sattari P, Martinuzzi RJ (2011) Alternating half-loop shedding in the turbulent wake of a finite surface-mounted square cylinder with a thin boundary layer. *Phys Fluids* 23:095101. doi:10.1063/1.3623463
- Caridi GCA, Ragni D, Sciacchitano A, Scarano F (2015) A seeding system for large-scale Tomographic PIV in aerodynamics. In: 11th international symposium on particle image velocimetry, Santa Barbara, USA
- de Kat R, van Oudheusden BW (2012) Instantaneous planar pressure determination from PIV in turbulent flow. *Exp Fluids* 52:1089–1106. doi:10.1007/s00348-011-1237-5
- Dobriloff C, Nitsche W (2009) Surface pressure and wall shear stress measurements on a wall mounted cylinder. In: Nitsche W, Dobriloff C (eds) *Imaging measurement methods*, NNFM 106. Springer, Berlin, pp 197–206
- Elsinga GE, Scarano F, Wieneke B, van Oudheusden BW (2006) Tomographic particle image velocimetry. *Exp Fluids* 41:933–947. doi:10.1007/s00348-006-0212-z
- Gesemann S, Huhn F, Schanz D, Schröder (2016) From noisy particle tracks to velocity, acceleration and pressure fields using B-splines and penalties. In: 18th international symposium on applications of laser and imaging techniques to fluid mechanics. Lisbon, Portugal, 4–7 July
- Ghaemi S, Scarano F (2010) Multi-pass light amplification for tomographic particle image velocimetry applications. *Meas Sci Technol* 21:127002. doi:10.1088/0957-0233/21/12/127002
- Ghaemi S, Scarano F (2013) Turbulent structure of high-amplitude pressure peaks within the turbulent boundary layer. *J Fluid Mech* 735:381–426. doi:10.1017/jfm.2013.501
- Hain R, Kähler CJ, Michaelis D (2008) Tomographic and time resolved PIV measurements on a finite cylinder on a flat plate. *Exp Fluids* 45:715–724. doi:10.1007/s00348-008-0553-x
- Jeon YJ, Earl T, Braud P, Chatellier L, David L (2016) 3D pressure field around an inclined airfoil by tomographic TR-PIV and its comparison with direct pressure measurements. In: 18th international symposium on the application of laser techniques to fluid mechanics. Lisbon, Portugal, 4–7 July
- Kähler CJ, Scharnowski S, Cierpka C (2012) On the resolution limit of digital particle image velocimetry. *Exp Fluids* 52:1629–1639. doi:10.1007/s00348-012-1280-x
- Kühn M, Ehrenfried K, Bosbach J, Wagner C (2011) Large-scale tomographic particle image velocimetry using helium-filled soap bubbles. *Exp Fluids* 50:929–948. doi:10.1007/s00348-010-0947-4
- Malik NA, Dracos Th, Papantoniou DA (1993) Experiments in fluids particle tracking velocimetry in three-dimensional flows part II: particle tracking. *Exp Fluids* 294:279–294. doi:10.1007/BF00223406
- Pattenden RJ, Turnock SR, Zhang X (2005) Measurements of the flow over a low-aspect-ratio cylinder mounted on a ground plane. *Exp Fluids* 39:10–21. doi:10.1007/s00348-005-0949-9
- Pröbsting S, Scarano F, Bernardini M, Pirozzoli S (2013) On the estimation of wall pressure coherence using time-resolved tomographic PIV. *Exp Fluids* 54:1567. doi:10.1007/s00348-013-1567-6
- Scarano F, Ghaemi S, Caridi GCA, Bosbach J, Dierksheide U, Sciacchitano A (2015) On the use of helium-filled soap bubbles for large-scale tomographic PIV in wind tunnel experiments. *Exp Fluids* 56:42. doi:10.1007/s00348-015-1909-7
- Schanz D, Gesemann S, Schröder A (2016) Shake the box: lagrangian particle tracking at high particle image densities. *Exp Fluids* 57:70. doi:10.1007/s00348-016-2157-1

- Schneiders JFG, Scarano F (2016) Dense velocity reconstruction from tomographic PTV with material derivatives. *Exp Fluids* 57:139. doi:[10.1007/s00348-016-2225-6](https://doi.org/10.1007/s00348-016-2225-6)
- Sumner D (2013) Flow above the free end of a surface-mounted finite-height circular cylinder: a review. *J Fluids Struct* 43:41–63. doi:[10.1016/j.jfluidstructs.2013.08.007](https://doi.org/10.1016/j.jfluidstructs.2013.08.007)
- Tropea C, Yarin A, Foss JF (2007) *Springer handbook of experimental fluid mechanics*. Springer, Berlin. ISBN 978-3-540-30299-5
- van Oudheusden BW (2013) PIV-based pressure measurement. *Meas Sci Technol* 24:032001. doi:[10.1088/0957-0233/24/3/032001](https://doi.org/10.1088/0957-0233/24/3/032001)
- Wieneke B (2013) Iterative reconstruction of volumetric particle distribution. *Meas Sci Technol* 24:024008. doi:[10.1088/0957-0233/24/2/024008](https://doi.org/10.1088/0957-0233/24/2/024008)